Temporally decoherent and spatially coherent vibrations in metal halide perovskites

Depei Zhang,[1,*,†] Xiao Hu,[1,*] Tianran Chen,[1,‡] Douglas L. Abernathy,[2] Ryoichi Kajimoto,[3] Mitsutaka Nakamura,[3] Maiko Kofu,[3] Benjamin J. Foley,[4] Mina Yoon,[5] Joshua J. Choi,[4] and Seung-Hun Lee[1,§]

[1]*Department of Physics, University of Virginia, Charlottesville, Virginia 22904, USA*
[2]*Neutron Scattering Division, Oak Ridge National Laboratory, Oak Ridge, Tennessee 37831, USA*
[3]*Materials and Life Science Division, J-PARC Center, Tokai, Ibaraki 319-1195, Japan*
[4]*Department of Chemical Engineering, University of Virginia, Charlottesville, Virginia 22904, USA*
[5]*Center for Nanophase Materials Sciences, Oak Ridge National Laboratory, Oak Ridge, Tennessee 37831, USA*

(Received 17 August 2020; revised 30 November 2020; accepted 1 December 2020; published 31 December 2020)

The long carrier lifetime and defect tolerance in metal halide perovskites (MHPs) are major contributors to the superb performance of MHP optoelectronic devices. Large polarons were reported to be responsible for the long carrier lifetime. Yet microscopic mechanisms of the large polaron formation, including the so-called phonon melting, are still under debate. Here, time-of-flight inelastic neutron scattering experiments and first-principles density-functional theory calculations were employed to investigate the lattice vibrations (or phonon dynamics) in methylammonium lead iodide, a prototypical example of MHPs. Our findings are that optical phonons lose temporal coherence gradually with increasing temperature which vanishes at the orthorhombic-to-tetragonal structural phase transition. Surprisingly, however, we found that the spatial coherence is still retained throughout the decoherence process. We argue that the temporally decoherent and spatially coherent vibrations contribute to the formation of large polarons in this metal halide perovskite.

DOI: 10.1103/PhysRevB.102.224310

I. INTRODUCTION

Metal halide perovskites (MHPs) have achieved striking success as low-cost photovoltaic and light-emitting devices [1–9]. Previous studies on MHPs suggest that their high performance in optoelectronic devices arises from the long carrier lifetimes, long carrier diffusion lengths, and exceptional carrier protection from defects [10–15]. Relevant underlying microscopic processes include polaron formation [16–23], exciton formation [24–30], electron-phonon coupling [25,31–36], and phonon melting [10,37]. For the three-dimensional (3D) hybrid organic-inorganic MHPs, it has been experimentally shown that the reorientation of the polarized molecules can assist the polaron formation, and thus prolong the charge carrier lifetime [21]. This was supported by a recent theoretical study based on the tight-binding model and first-principles density-functional theory calculations that reported increase of the polaron binding energy from 12 to 55 meV when molecular dynamic disorder is considered in addition to the electron-phonon coupling [19]. However, the purely inorganic MHPs without organic molecules can also achieve a moderate photovoltaic performance [38,39], which indicates that other mechanisms that are directly related to the inorganic perovskite framework must also play indispensable roles in the optoelectronic properties of MHPs through their interactions with the charge carriers. The two relevant principal mechanisms of the inorganic framework for the photovoltaic properties are electron-phonon coupling [25,31–36] and phonon melting [10,37].

Electron-phonon coupling, i.e., the interaction between the charge carriers and the lattice vibrations, has been shown experimentally to affect various optical and electrical properties of MHPs. For example, a thermally induced blueshift of the band gap was attributed to the population of a 1-THz optical Pb-I-Pb bending mode in methylammonium lead iodide ($MAPbI_3$) [40]. Also, the thermally induced changes in the line shape, linewidth, and intensity of the photoluminescence spectrum in various two-dimensional (2D) lead iodide perovskites were attributed to electron-phonon coupling [36]. Previous studies indicate that at room temperature the electron-phonon couplings in MHPs occur through the longitudinal optical (LO) phonons, such as the Pb-I-Pb bending or Pb-I stretching modes [25,31,40]. Zhu and colleagues (Miyata *et al.* [10,17]) argued that such electron-phonon coupling in 3D MHPs leads to the formation of large polarons which then protect the charge carriers from the defects and impurities.

The so-called phonon melting describes a phenomenon in which the phonon peaks that are well defined in energy at low temperatures broaden upon heating and eventually become a featureless continuum at high temperatures even though the system remains crystalline. The phonon melting, or more strictly, time-decoherent phonons, in MHPs [37,41–46], are due to the intrinsic softness of their ionic crystals. The optical phonon "overdamping" feature in multiple MHPs was reported in Ref. [43], which attributes the gradual "melting" behavior of low-energy optical modes to the

*These authors contributed equally to this work.
†Present address: Neutron Scattering Division, Oak Ridge National Laboratory, Oak Ridge, TN 37831, USA.
‡Present address: NIST Center for Neutron Research, National Institute of Standards and Technology, Gaithersburg, MD20899, USA.
§Corresponding author: shlee@virginia.edu

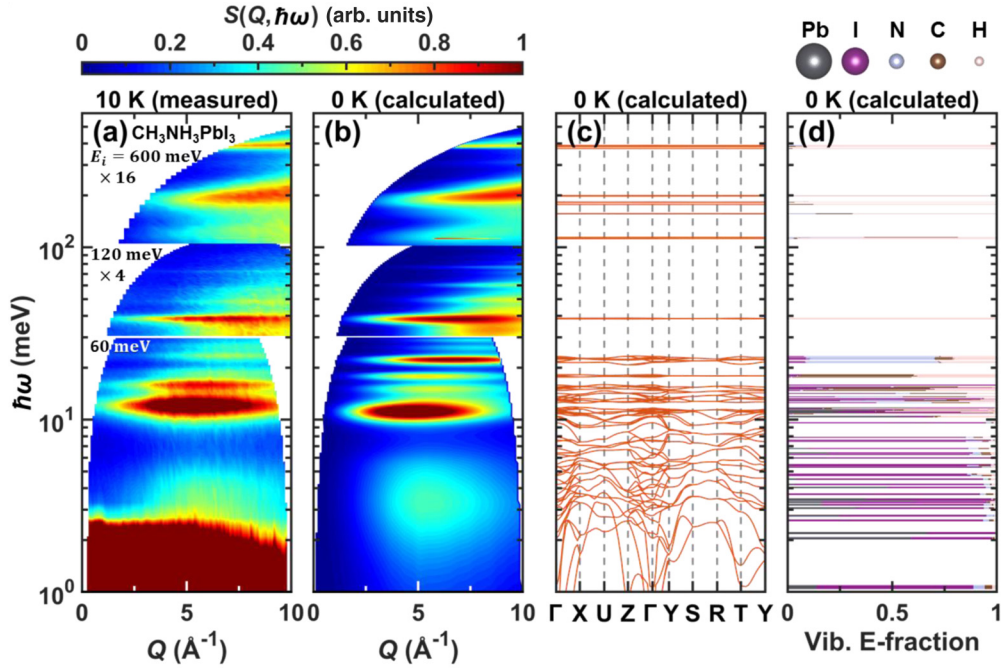

FIG. 1. Phonon spectra of $CH_3NH_3PbI_3$. (a), (b) Color contour maps of the experimental (a) and calculated (b) phonon spectra $S(Q,\ \hbar\omega)$ of $CH_3NH_3PbI_3$ as a function of the linear momentum transfer Q and the log-scale energy transfer $\hbar\omega$. For better visualization of the entire range of phonon spectra up to ~400 meV, $S(Q,\ \hbar\omega)$ obtained with three different incident neutron energies, $E_i = 60$, 120, and 600 meV, are multiplied by different factors, 1, 4, and 16, respectively. (b) DFT phonon spectra calculated for the low-T orthorhombic phase of $CH_3NH_3PbI_3$. (c) DFT phonon band structure of orthorhombic $CH_3NH_3PbI_3$ along high-symmetry Q points. (d) Vibrational energy fractions (Vib. E-fraction) at the Γ point for each phonon mode of $CH_3NH_3PbI_3$, (see the Supplemental Material, Session F.1 [56] for the calculation details). The widths of the gray, violet, cyan, brown, and pink bars represent the energy fractions of the Pb, I, N, C, and H atoms, respectively.

phonon anharmonicity. However, the temperature range of their study was very limited, from 5 to 120 K, covering only the low-temperature structural phase and leaving out the structural phase transition to the higher-temperature structural phase.

When the phonons are decoherent in time, the system still remains crystalline. It is called the crystal-liquid duality, which leads to the "bandlike" charge carrier dynamics and glasslike phonons [10]. It was also argued that the glasslike phonon modes can further assist the optoelectronic performances in MHPs through their participation in the large polaron formation and hot carrier cooling processes [10]. Understanding the microscopic nature of the crystal-liquid duality and how it affects the optoelectronic properties of MHPs requires systematic studies of vibrational dynamics in MHPs as a function of temperature covering all the structural phases.

Here, we employ the time-of-flight (TOF) inelastic neutron scattering (INS) experiments and first-principles density-functional theory (DFT) calculations to investigate how the phonon dynamics of a 3D MHP, $MAPbI_3$, is involved with temperature, covering its three different structural phases. Our study showed that optical phonons lose temporal coherence gradually with increasing temperature which nearly vanishes at the orthorhombic-to-tetragonal phase transition. During the temporal decoherence process, however, the spatial coherence is still retained. We argue that the liquidlike temporal decoherence and the crystalline spatial coherence of optical phonons yield both higher polarizability and spatial extension of a localized phonon packet to form large polarons in this 3D lead halide perovskite.

II. RESULTS

A. Momentum and energy dependence of phonon spectra

The time-of-flight neutron scattering experiments were performed on an 8-g powder sample of $CH_3NH_3PbI_3$ to examine the vibrational motions. Figure 1(a) shows a color contour map of the neutron scattering cross section $S(Q, \hbar\omega)$ as a function of momentum transfer Q and energy transfer $\hbar\omega$, taken at 10 K. The phonon spectra are roughly composed of three regions: (i) the low-energy part (0−10 meV), the mostly inorganic modes, denoted as inorganic modes, which mostly involve the collective vibrations of inorganic atoms, including the Pb-I-Pb translation and Pb-I-Pb bending modes [47–49]; (ii) the intermediate energy part (10−30 meV), the organic-inorganic hybrid modes, denoted as hybrid modes, which are mixture modes of the inorganic motions, mainly the Pb-I-Pb rocking and Pb-I-Pb stretching, and the molecular rigid-body motions, i.e., CH_3NH_3 translation, spinning and libration; and (iii) the high-energy part (30−400 meV), the nearly pure organic-atom vibrations, denoted as organic modes, which are dominated by the internal molecular motions, e.g., CH_3NH_3 twisting (or torsion), bending, rocking, stretching, and deformation.

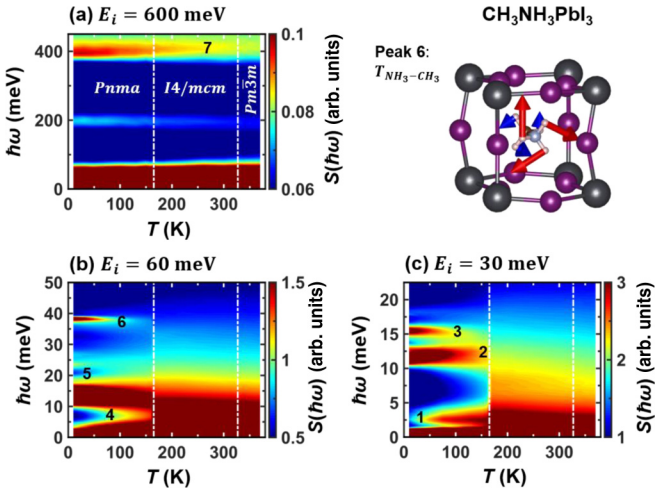

FIG. 2. Temperature-dependent phonon spectra of $CH_3NH_3PbI_3$. (a)–(c) Color contour maps of Q-integrated neutron scattering intensity, $S(\hbar\omega) = \int S(Q, \hbar\omega)dQ / \int dQ$, as a function of temperature T and $\hbar\omega$, taken at 20 different temperatures while heating from 10 to 370 K, with the incident neutron energy E_i of 600 meV (a), 60 meV (b), and 30 meV (c). The vertical dash-dotted lines in (a)–(c) represent the transition temperatures for the orthorhombic (*Pnma*)-to-tetragonal (*I*4/*mcm*) and tetragonal (*I*4/*mcm*)-to-cubic ($Pm\bar{3}m$) phase transitions, at 165 and 327 K, respectively. Phonon peaks and valleys are labeled as 1–7 for further analysis. The top right panel illustrates the $T_{NH_3-CH_3}$ twisting mode, which corresponds to the phonon peak 6.

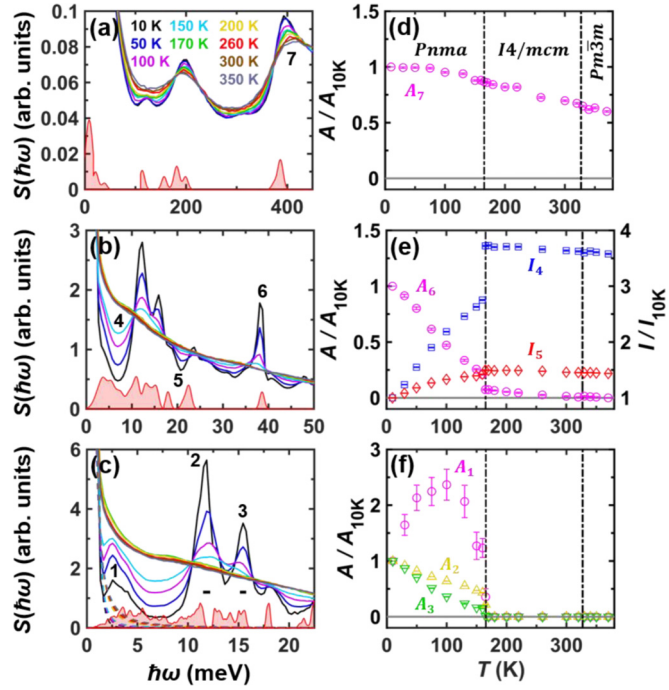

FIG. 3. Temperature-dependent phonon spectra of $CH_3NH_3PbI_3$. (a)–(c) The line plots of the $S(\hbar\omega)$ for nine selected temperatures, 10, 50, 100, 150 K (low-T orthorhombic phase); 170, 200, 250, 300 K (intermediate-T tetragonal phase); and 350 K (high-T cubic phase), taken with E_i = 600 meV (a), E_i = 60 meV (b), and E_i = 30 meV (c). The red lines with shaded areas at the bottom of panels (a)–(c) are the calculated phonon density of states (PDOSs) with the vdW-DF2 correction [55], respectively. The dashed lines in (c) represent the contributions from the CH_3NH_3 molecule rotations, for all nine temperatures in the corresponding colors. The black horizontal bars in (c) represent the full width at half maximum (FWHM) of the instrument resolution for peaks 2 and 3. (d)–(f) show the temperature dependence of the fitted Gaussian peak areas, A, of phonon modes 1–3, 6 and 7, as labeled in (a)–(c). The fitted area A is normalized by the peak area of 10 K, $A_{10\,K}$. In (e), the blue squares and red diamonds show the integrated intensity I of the phonon valley 4 ($6 \leqslant \hbar\omega \leqslant 8$ meV) and 5 ($20 \leqslant \hbar\omega \leqslant 22$ meV) labeled in (b), which are normalized by the values at 10 K, $I_{10\,K}$. The vertical dash-dotted lines in (d)–(f) represent the transition temperatures for the orthorhombic (*Pnma*)-to-tetragonal (*I*4/*mcm*) and tetragonal (*I*4/*mcm*)-to-cubic ($Pm\bar{3}m$) phase transitions, at 165 and 327 K, respectively.

The identification of phonon modes for the experimentally measured peaks using DFT calculations and molecular dynamics (MD) has been challenging [50,51]. We found that long-range van der Waals (vdW) interactions play a critical role in capturing the key features of experimental phonon spectra of $MAPbI_3$; we found that the nonlocal correction to DFT total energy using van der Waals density functional schemes, such as vdW-DF2 [52–55], needs to be included to reproduce the phonon spectra for $MAPbI_3$. For instance, the antisymmetric twisting mode of NH_3 and CH_3, $T_{NH_3-CH_3}$, illustrated in Fig. 2, shifts to a lower energy by ∼8 meV [the red-shaded curve on the bottom of Fig. 3(b)] explaining the experimental data, compared to when vdW interactions are not included (see Fig. S5 in the Supplemental Material (SM) [56]). Detailed information on the vibrational modes, including their energies and animations, and density of states as a function of energy, are shown on the website of one of the authors (Lee [57]).

Our DFT calculations with the vdW-DF2 correction estimated the London dispersion interactions between the organic MA^+ molecule and its neighboring inorganic $[PbI_3]^-$ layer to be $E_{vdW}^{MA^+-[PbI_3]^-} \approx -0.912$ eV which is ∼13.4% of the total electronic energy between the two components. Thus, it is not surprising that the London dispersion interaction with a distance dependence of $\frac{1}{r^6}$ [58] has a significant influence on the restoring force, and hence the phonon energy, of the antisymmetric twisting mode of the NH_3 and CH_3 group of the MA^+ molecule.

The inelastic neutron scattering intensities due to the vibrational motions were calculated for $MAPbI_3$, using the density functional theory calculations (see the Supplemental Material, Session F.1 [56], for details). As shown in Fig. 1(b), the powder-averaged calculated intensities reproduce well the measured ones shown in Fig. 1(a), on both the Q and $\hbar\omega$ dependences. The experimental observation, shown in Figs. 1(a) and 3(b), that the peak centered at 11.7(1) meV is significantly broader than the one at 38.2(1) meV, is also reproduced. As shown in the calculated phonon dispersion relations and vibrational energy fraction shown in Figs. 1(c) and 1(d), respectively, this difference is due to the fact that the 11.7-meV mode is a collection of hybrid modes that are dispersive along high-symmetric directions in Q space while the 38.2-meV mode is the lowest-energy vibrational mode of the MA molecule internal motion and is very weakly dispersive even in the crystal. We stress that the Q and $\hbar\omega$ dependences

of $S(Q, \hbar\omega)$ measured at 10 K are well reproduced by the calculations, and the dispersiveness of the hybrid modes at intermediate energies and of the inorganic modes at low energies is clear evidence that the hybrid and inorganic modes are strongly collective; in other words, those vibrations are spatially and temporally coherent at 10 K.

B. Energy dependence of phonon spectra and temporal decoherence

Now let us see how the phonon spectrum changes with increasing temperature. Figures 2(a)–2(c) show contour maps of the momentum-integrated neutron scattering intensity $S(T,\ \hbar\omega)$ as a function of temperature T and energy transfer $\hbar\omega$ that show the temperature evolution of the vibrational dynamics of $MAPbI_3$ over the entire energy range up to ~400 meV. As discussed before and shown as the black curves in Fig. 3(a)–3(c), at 10 K [orthorhombic phase ($Pnma$)], there exist temporally and spatially coherent vibrational modes over the entire energy range. However, the peaks below 50 meV become featureless in energy above the orthorhombic-to-tetragonal phase transition at ~165 K [see Figs. 3(b) and 3(c)]. This indicates that the optical inorganic and hybrid vibrational motions lose coherence in time; i.e., those phonons are melted in the tetragonal ($I4/mcm$) and cubic ($Pm\bar{3}m$) phases above 165 K. In the orthorhombic phase below 165 K, the two types of modes behave differently; the optical inorganic modes, denoted by A_1 (mainly the Pb-I-Pb bending modes), increase in strength as T increases up to 100 K above which they weaken and melt as the system enters the tetragonal phase at 165 K [see Figs. 3(c) and 3(f)]. The hybrid modes, denoted by A_2 (the mixed modes of rocking and stretching of Pb-I-Pb and translation and spinning of CH_3NH_3) and A_3 (the mixed modes of stretching of Pb-I-Pb and translation and libration of CH_3NH_3), on the other hand, gradually decrease in strength as T increases and then melt in the tetragonal phase [see Figs. 3(c) and 3(f)]. The organic modes, denoted by A_6 [CH_3-NH_3 twisting (or torsion) modes] in Figs. 3(b) and 3(e), and A_7 (symmetric and asymmetric stretching modes of CH_3 and NH_3) in Figs. 3(a) and 3(d), behave differently; upon warming the 38.2-meV mode, A_6, gradually weakens and melts at 155 K, similar to the way the hybrid modes do. On the other hand, the 400-meV mode, A_7, gradually broadens but survives all the way to the cubic phase. These different behaviors can be understood when one considers the charge distribution in the MA^+ molecule. In the MA^+ molecule the overall positive charge is mainly distributed in the $NH_3{}^+$ group and the CH_3 group is more or less neutral [21]. In the 38.2-meV mode, A_6, $NH_3{}^+$ twists twice more than CH_3 does (the amplitude ratio of $NH_3{}^+ : CH_3 = 2.2 : 1$) as illustrated in Fig. 2, top right panel, and thus the mode gets affected as the motion of the neighboring negative I^- ions melts upon warming. The higher-energy organic modes such as A_7, on the other hand, involve the equal strength motion of CH_3 and NH_3, and thus get less affected by the melting of the inorganic and hybrid modes. See the detailed phonon animations on Lee's website [57].

The observed energy continuum up to ~50 meV is an indication of the emergence of liquidlike vibrations upon heating, i.e., the temporally decoherent phonons. To study the T dependence of the liquidlike vibrations, we have chosen the valley regions at $6 \leqslant \hbar\omega \leqslant 8$ meV (I_4) and $20 \leqslant \hbar\omega \leqslant 22$ meV (I_5) where intensity is weak at 10 K [see Fig. 3(b)]. As shown in Fig. 3(e), I_4 (blue squares) and I_5 (red diamonds) show a gradual increase as T increases within the low-T orthorhombic phase. One can ask if the energy continuum is due to the contribution from the incoherent rotational dynamics as each MA^+ molecule rotates more freely as T increases. To quantitatively examine this possibility, we have fitted the very low-energy $S(Q,\ \hbar\omega)$ to the previously reported point group theory analysis for the rotational dynamics of the MA^+ molecule [59]. As described in the Supplemental Material, Session C [56], in detail, the rotational contributions can be determined. The color-coded dashed lines in Fig. 3(c) are the rotational contributions at different temperatures, clearly showing that the energy continuum up to 50 meV is indeed mainly due to the melting of the inorganic and hybrid vibrational dynamics rather than rotational dynamics. Similar measurements were performed on a partially deuterated $MAPbI_3$ sample ($CD_3NH_3PbI_3$), where the incoherent scattering from H atoms is suppressed, and the same liquidlike vibrations were observed at high temperatures. As shown in Fig. S4 in the Supplemental Material [56], the temperature evolution of the inorganic and hybrid modes ($A_{1'}$ and $A_{2'}$ in Fig. S4 [56]) of the partially deuterated sample is consistent with that of nondeuterated sample [Fig. 3(f)].

The lifetimes of different types of phonons were evaluated as follows (for details, see the Supplemental Material, Sessions D and E [56]). We fitted the $E_i = 10$ and 30 meV data sets separately using the Voigt function $V(x-\mu;\sigma,\gamma)$ for each phonon peak. To minimize the number of fitting parameters and thus to increase the reliability of the analysis, we introduce two lifetimes only to account for the optical inorganic and hybrid modes, assuming that all the inorganic modes have the same lifetime and all the hybrid modes have another similar lifetime. This is a reasonable assumption because the inorganic modes involve Pb-I-Pb bending and weaker vibrations of the organic molecule while the hybrid modes involve Pb-I-Pb stretching with stronger vibrations of the molecule. The fitting results are shown in Figs. 4(a) and 4(b), and the fitted parameters are shown in Fig. 5(a) and summarized in Table I. Our analysis shows that both the lifetimes of inorganic phonons and hybrid phonons decrease with the temperature increasing and the lifetime of hybrid phonons decreases much faster than that of inorganic phonons.

C. Momentum dependence of phonon spectra and spatial coherence

A question that naturally arises is what happens to the spatial coherence of the collective vibrations when the inorganic phonons and the hybrid phonons lose their coherence in time. To address this issue, we investigate the Q dependences of the vibrational modes $S(Q)$ for $MAPbI_3$ as a function of temperature. Figures 6(a)–6(c) show the color contour maps of $S(Q, \hbar\omega)$ taken with $E_i = 60$ meV, covering the inorganic and the hybrid modes, at three different temperatures, 10, 170,

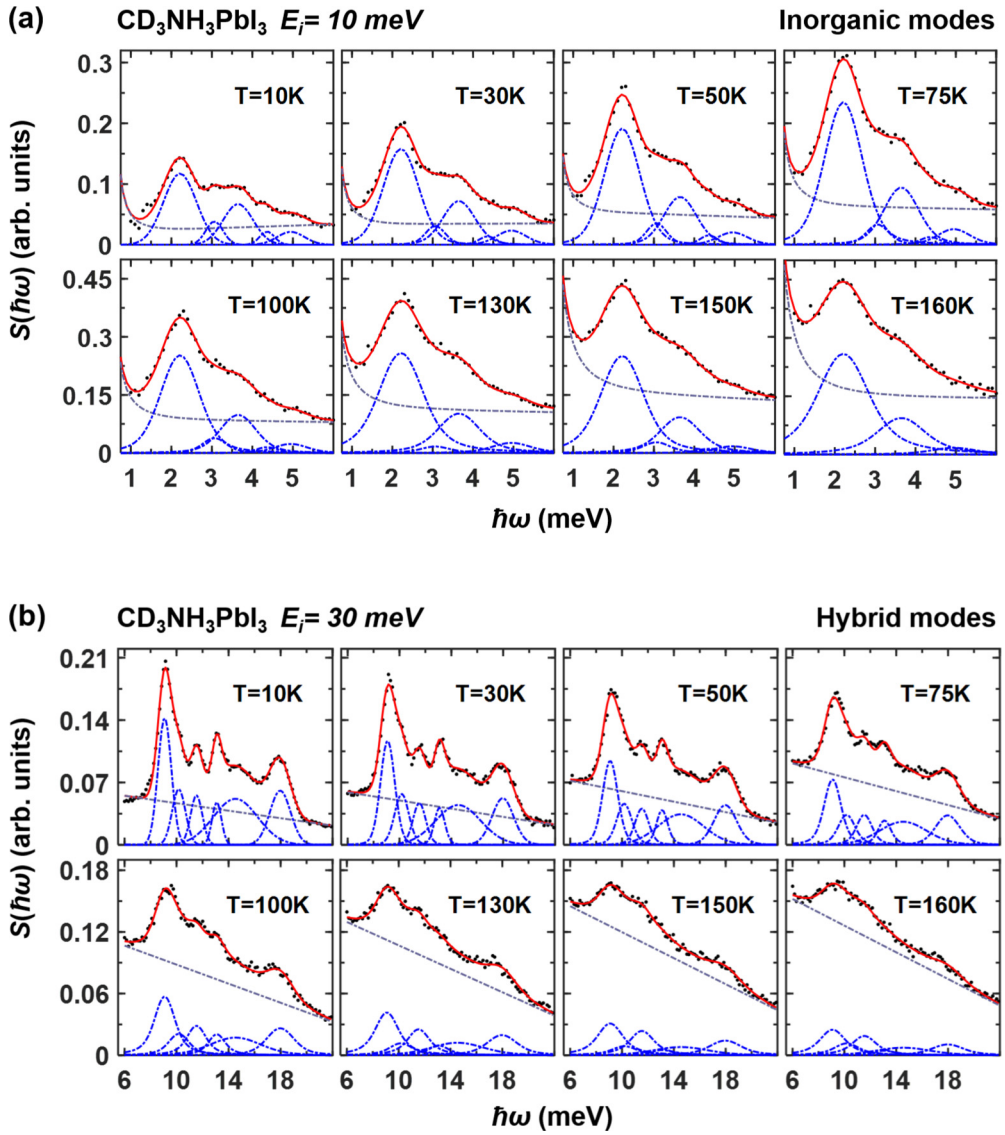

FIG. 4. Phonon spectra of $CD_3NH_3PbI_3$. The momentum-integrated experimental phonon spectra (black dots), $S(\hbar\omega)$, were collected at the time-of-flight spectrometer 4SEASONS at JPARC with two incident neutron energies $E_i = 10$ meV and $E_i = 30$ meV. (a) For the inorganic modes, the phonon spectra were fitted with five Voigt functions (blue dashed lines on the bottom). The gray dashed lines account for the increasing rotational contributions and liquidlike continuum with increasing temperature. (b) For the hybrid modes, the rotational contribution in the fitted energy range is negligible. The phonon spectra were fitted with six Voigt functions (blue dashed lines). The gray dashed lines account for the liquidlike continuum with increasing temperature. In (a), (b), the red solid lines are the fitted total intensities.

and 350 K, respectively. At 10 K, $S(Q, \hbar\omega)$ exhibits well-separated peaks in $\hbar\omega$ that are broad and centered at around $Q \sim 5 - 7\,\text{Å}^{-1}$. At 170 and 350 K, $S(Q, \hbar\omega)$ exhibits an energy continuum, as discussed, due to the temporal decoherence. Surprisingly, however, the energy continuum exhibits Q dependence similar to that of the temporally coherent phonons observed at 10 K.

In order to quantitatively analyze the data, we integrated $S(Q, \hbar\omega)$ over three different $\hbar\omega$ regions to cover the inorganic and hybrid modes at the low-energy and intermediate-energy regions, respectively. The resulting $S(Q)$ is plotted in Figs. 6(d)–6(f). Upon heating, all the resulting $S(Q)$ exhibit a gradual shift to lower Q, which is due to the increasing vibrational amplitudes. In addition, for the low-energy range of 2 meV $< \hbar\omega <$ 5 meV shown in Fig. 6(d), in the tetragonal phase ($T >$ 165 K) $S(Q)$ exhibits an additional peak centered at lower $Q \sim 2\text{Å}^{-1}$ which is due to the rotational dynamics of the MA^+ molecule and is well reproduced by the aforementioned group theoretical model for the rotational dynamics, $S_{\text{rot}}(Q)$, shown as the color-coded dashed lines. For other higher-energy regions, the rotational contribution is negligible. We have fitted the vibrational contribution $S_{\text{vib}}(Q) = S(Q) - S_{\text{rot}}(Q)$ to a phenomenological function for phonons $S_{\text{model}}(Q, T) = a + bS_{\text{calc}}(Q, 0\,\text{K})e^{-\Delta U_{\text{iso}}Q^2}$, with the precalculated phonon intensity at 0 K using OCLIMAX [60]; $S_{\text{calc}}(Q,\ 0\,\text{K})$; and the constant background a, the intensity amplitude b, and in the Debye-Waller factor $e^{-\Delta U_{\text{iso}}Q^2}$, $\Delta U_{\text{iso}} = U_{\text{iso}}(T) - U_{\text{iso}}(0\,\text{K})$, with $U_{\text{iso}}(T)$ representing the T-dependent isotropic atomic displacement parameter, which is proportional to the square of the vibrational amplitude.

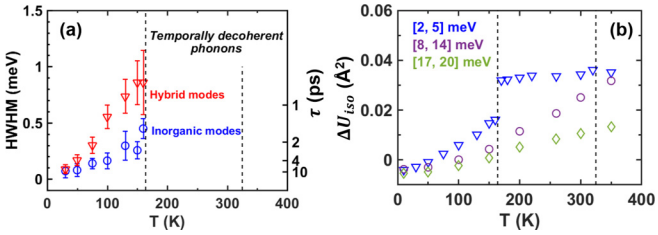

FIG. 5. Temperature-dependent phonon lifetime and atomic displacement parameters of $MAPbI_3$. (a) The blue circles and the red triangles are the phonon energy linewidth and lifetime of the inorganic and hybrid modes, respectively, obtained from fitting $S(\hbar\omega)$ in Fig. 4. (b) The atomic displacement parameters, $\Delta U_{\rm iso} = U_{\rm iso}(T) - U_{\rm iso}(0\ K)$, were obtained from fitting $S(Q)$ in Figs. 6(d)–6(f) as described in the text. $\Delta U_{\rm iso}$ are determined and plotted for three different $\hbar\omega$ regions: $2 \leqslant \hbar\omega \leqslant 5$ meV ($E_i = 30$ meV, blue triangles), $8 \leqslant \hbar\omega \leqslant 14$ meV ($E_i = 60$ meV, violet circles), and $17 \leqslant \hbar\omega \leqslant 20$ meV ($E_i = 60$ meV, green diamonds).

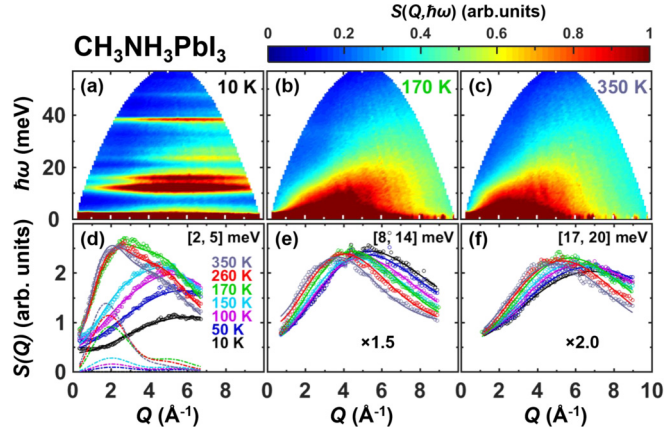

FIG. 6. Inelastic neutron scattering spectra and Q dependence of the phonon spectra for $MAPbI_3$. (a)–(c) The color contour maps of $S(Q, \hbar\omega)$ of $CH_3NH_3PbI_3$ taken at 10 K (orthorhombic phase), 170 K (tetragonal phase), and 350 K (cubic phase) with the incident neutron energy $E_i = 60$ meV. (d)–(f) The colored circles are the $\hbar\omega$-integrated neutron scattering intensity, $S(Q)$, for seven different temperatures, taken with the incident neutron energies $E_i = 30$ meV (d) and $E_i = 60$ meV [(e), (f) The $\hbar\omega$ integration region was $2 \leqslant \hbar\omega \leqslant 5$ meV (d), $8 \leqslant \hbar\omega \leqslant 14$ meV (e), and $17 \leqslant \hbar\omega \leqslant 20$ meV (f), respectively. In (d), the rotational contributions are shown as dashed lines and the total fitted intensities are shown as solid lines, as discussed in the text. The panels (e), (f) are rescaled by a factor of 1.5 and 2.0, respectively, to have the same scale as the panel (d).

As shown as the color-coded solid lines in Figs. 6(d)–6(f), $S_{\rm model}(Q)$ can reproduce the experimental $S(Q)$ for all the three energy regions and all the temperatures. The fitted isotropic thermal factors, $\Delta U_{\rm iso}$s, are shown in Fig. 5(b). Here, we emphasize that the experimental $S(Q)$ cannot be explained if the optical phonons completely lose the spatial coherence. It is because in the case of spatially decoherent vibrations of Pb and I atoms $S(Q)$ should exhibit a peak centered at a much higher $Q > 10$ Å^{-1} as expected for the localized vibrations of individual atoms [61]. Instead, our observation that $S_{\rm model}(Q)$ for the spatially coherent vibrations at 10 K weighted by the Debye-Waller factor can also account for the Q dependence of vibrations at high T s means that the optical vibrations at high T s are coherent in space even though the vibrational amplitude increases with T. This tells us that when the optical vibrational modes start losing coherence due to the weak ionic bonds, which will be discussed later, upon heating, the decoherence occurs first in time and the spatial coherence remains at high T s.

III. DISCUSSION

To understand the origin of the phonon melting behaviors observed in $MAPbI_3$, we calculated the binding energy between nearest-neighboring atoms for three different systems, $CH_3NH_3PbI_3$, another ionic crystal NaCl, and a covalent crystal SiO_2 for comparison (see the Supplemental Material, Session F.2 [56], for details). The binding energies between inorganic atoms in the two ionic crystals have a binding energy of ∼3–4 eV that is much weaker than the bonding energy of ∼10 eV of the covalent crystal SiO_2. The intramolecule bonding energies of the organic molecules of MHPs, such as the N-C and C-C bonding energies of ∼9 and ∼7 eV, respectively, are comparable to that of SiO_2, which is expected because the intramolecule bonds are covalent. Thus, the gradual phonon melting, i.e., the T-induced temporal decoherence observed for the low-energy vibrations in $MAPbI_3$, is due to the weak ionic bonds between the inorganic atoms in MHPs. The survival of the time coherence of the purely organic high-energy vibrational modes at room temperature, on the other hand, is due to the strong covalent intramolecule bonds. Furthermore, we have simulated the

TABLE I. Estimated phonon lifetimes of the inorganic and hybrid phonon modes in the orthorhombic phase of $CD_3NH_3PbI_3$, extracted from the phonon model fittings on data taken at JPARC. Values in the parentheses indicate their errors.

	Inorganic modes		Hybrid modes	
T (K)	Lorentzian HWHM (meV)	Phonon lifetime (ps)	Lorentzian HWHM (meV)	Phonon lifetime (ps)
160	0.45(9)	1.47	0.86(28)	0.77
150	0.26(8)	2.58	0.86(20)	0.77
130	0.30(13)	2.22	0.74(15)	0.90
100	0.16(7)	4.07	0.55(10)	1.19
75	0.14(5)	4.76	0.30(7)	2.20
50	0.08(6)	8.19	0.17(5)	3.90
30	0.07(6)	9.57	0.08(4)	7.50

powder-averaged phonon spectra of the three systems as a function of the temperature (see the Supplemental Material, Session F.3 [56], for details). As shown in Fig. S6 [56], the temperature-dependent phonon spectra simulations show that the gradually decreasing phonon intensities, i.e., the phonon melting behavior, is a general feature for the ionic lattices with the weak ionic bonds. The phonon modes, in the covalent lattices, e.g., SiO_2, on the other hand, can survive at high temperatures. It should be noted that the rotational dynamics of the organic molecule may also enhance the phonon melting, as the C_4 mode of the MA^+ cation gets activated when the system enters the intermediate-temperature tetragonal phase from the low-temperature orthorhombic phase [59]. However, it is to be emphasized that the MA^+ C_4 rotational mode requires breaking of the multiple bonds between iodine and hydrogen atoms and thus its activation is a direct outcome of the weak ionic I-H bonds.

Note that $MAPbI_3$ is crystalline up to 650 K [62]. Thus, according to the Goldstone theorem the very low-energy acoustic phonons below ∼2 meV should exist as long as the system is crystalline. Indeed, a recent experimental study reported the existence of temporally and spatially coherent acoustic phonons in $MAPbI_3$ at 350 K [63]. Our experimental results, on the other hand, showed that for the optical inorganic and hybrid phonons the temporal coherence is lost for $T > 165\ \text{K} \ll 650\ \text{K}$, which is consistent with previous Raman and neutron scattering studies on isostructural systems $MAPbX_3$ ($X = \text{Br}$ [37,41], Cl [42]). More strikingly, we have shown that those optical phonons retain spatial coherence. The observed spatial coherence of the optical phonons above 165 K may explain the previous results that phonon-mediated large polarons are formed in 3D MHPs, and the diameter of the polarons was theoretically determined for 3D MHPs to be ∼50 Å [19] and was experimentally determined to be ∼100–140 Å in terms of an exciton picture [64]. Previous optical measurement studies, such as Raman scattering, photoluminescence, and terahertz spectroscopy, showed that the electron-phonon couplings in MHPs occur through the optical phonons, such as the Pb-I-Pb bending and Pb-I stretching modes at room temperature [25,31,40]. For a phonon to form a polaron, the spatial coherence of the phonon should be larger than or at least comparable to the size of the polaron. These imply that the optical inorganic and hybrid phonons of $MAPbI_3$ must be spatially coherent at least over ∼50 Å, which is consistent with our findings. Indeed, a theoretical study based on molecular dynamics simulations on anharmonic materials [65] showed that the temporal coherence and the spatial coherence of phonons can behave differently. Their argument is the following: The temporal coherence is associated with the phonon mean free path, i.e., the product of the phonon relaxation time and group velocity, reflecting the particle nature of phonons, which is consistent with the low thermal conductivities of MHPs [51,66–70]. On the other hand, the spatial coherence represents the spatial extension of a localized phonon packet reflecting the wave nature of the phonons. They showed that at some specific points in the Brillouin zone, the difference between the phonon mean free path and spatial extension can be giant, and even when the mean free path becomes very small, the spatial extension can be large, yielding a nonlocalized standing wave. Our neutron scattering results are an experimental observation of distinct temporal and spatial coherence of phonons.

The concept of the crystal-liquid duality has been actively studied in the family of solids called phonon-glass electron crystals (PGECs), such as intermetallic clathrates, that exhibit high electrical conductivity but low thermal conductivity, and thus provide good candidates for efficient thermoelectric materials [10,71]. Indeed, very recently the thermal conductivity of MHPs was found to be one of the lowest among all measured solid materials [72]. It would be interesting to see if the distinct temporal and spatial coherences of phonons found in MHPs are also a characteristic of PGECs that is involved in the microscopic mechanism of their thermoelectric properties.

All data are available in the paper or the Supplemental Material [56].

ACKNOWLEDGMENTS

The work at the University of Virginia was supported by the US Department of Energy, Office of Science, Office of Basic Energy Sciences under Award No. DE-SC0016144. A portion of this research used resources at the Spallation Neutron Source, a DOE Office of Science User Facility operated by the Oak Ridge National Laboratory. The neutron scattering experiments at the Material and Life Science Experimental Facility, Japan Proton Accelerator Research Complex, were performed under a user program (Proposal No. 2019B0011). A portion of computational work was conducted at the Center for Nanophase Materials Sciences which is a DOE Office of Science User Facility. This research used resources of the National Energy Research Scientific Computing Center (NERSC), a US Department of Energy Office of Science User Facility operated under Contract No. DE-AC02-05CH11231.

S.-H.L. designed the research; D.Z., X.H., T.C., D.L.A., R.K., M.N., M.K., B.J.F., M.Y., J.J.C., and S.-H.L. performed the research; D.Z., X.H., and T.C. analyzed data; and D.Z., X.H., J.J.C., and S.-H.L. wrote the paper.

The authors have no competing interests.

[1] T. Baikie, Y. Fang, J. M. Kadro, M. Schreyer, F. Wei, S. G. Mhaisalkar, M. Graetzel, and T. J. White. Synthesis and crystal chemistry of the hybrid perovskite $(CH_3NH_3)PbI_3$ for solid-state sensitised solar cell applications, J. Mater. Chem. A **1**, 5628 (2013).

[2] W. Xu, Q. Hu, S. Bai, C. Bao, Y. Miao, Z. Yuan, T. Borzda, A. J. Barker, E. Tyukalova, Z. Hu, M. Kawecki, H. Wang, Z. Yan, X. Liu, X. Shi, K. Uvdal, M. Fahlman, W. Zhang, M. Duchamp, J.-M. Liu *et al.*, Rational molecular passivation for high-performance perovskite light-emitting diodes. Nat. Photonics **13**, 418 (2019).

[3] T. M. Brenner, D. A. Egger, L. Kronik, G. Hodes, and D. Cahen. Hybrid organic-inorganic perovskites: Low-cost semiconductors with intriguing charge-

transport properties, Nat. Rev. Mater. **1**, 15007 (2016).
[4] NREL, Best Research-Cell Efficiencies, National Renewable Energy Laboratory (2020).
[5] D. Bi, C. Yi, J. Luo, J.-D. Décoppet, F. Zhang, S. M. Zakeeruddin, X. Li, A. Hagfeldt, and M. Grätzel, Polymer-templated nucleation and crystal growth of perovskite films for solar cells with efficiency greater than 21%. Nat. Energy **1**, 16142 (2016).
[6] E. H. Jung, N. J. Jeon, E. Y. Park, C. S. Moon, T. J. Shin, T.-Y. Yang, J. H. Noh, and J. Seo, Efficient, stable and scalable perovskite solar cells using poly (3-hexylthiophene), Nature **567**, 511 (2019).
[7] J. Tong, Z. Song, D. H. Kim, X. Chen, C. Chen, A. F. Palmstrom, P. F. Ndione, M. O. Reese, S. P. Dunfield, O. G. Reid, J. Liu, F. Zhang, S. P. Harvey, Z. Li, S. T. Christensen, G. Teeter, D. Zhao, M. M. Al-Jassim, M. F. A. M. van Hest *et al.*, Carrier lifetimes of >1 μs in Sn-Pb perovskites enable efficient all-perovskite tandem solar cells, Science **364**, 475 (2019).
[8] W. S. Yang, B.-W. Park, E. H. Jung, N. J. Jeon, Y. C. Kim, D. U. Lee, S. S. Shin, J. Seo, E. K. Kim, J. H. Noh, and S. I. Seok, Iodide management in formamidinium-lead-halide-based perovskite layers for efficient solar cells, Science **356**, 1376 (2017).
[9] N.-G. Park, M. Grätzel, T. Miyasaka, K. Zhu, and K. Emery, Towards stable and commercially available perovskite solar cells, Nat. Energy **1**, 16152 (2016).
[10] K. Miyata, T. L. Atallah, and X. Y. Zhu, Lead halide perovskites: Crystal-liquid duality, phonon glass electron crystals, and large polaron formation, Sci. Adv. **3**, e1701469 (2017).
[11] G. Xing, N. Mathews, S. Sun, S. S. Lim, Y. M. Lam, M. Grätzel, S. Mhaisalkar, and T. C. Sum, Long-range balanced electron- and hole-transport lengths in organic-inorganic $CH_3NH_3PbI_3$, Science **342**, 344 (2013).
[12] Q. Dong, Y. Fang, Y. Shao, P. Mulligan, J. Qiu, L. Cao, and J. Huang, Electron-hole diffusion lengths >175 μm in solution-grown $CH_3NH_3PbI_3$ single crystals, Science **347**, 967 (2015).
[13] D. Shi, V. Adinolfi, R. Comin, M. Yuan, E. Alarousu, A. Buin, Y. Chen, S. Hoogland, A. Rothenberger, K. Katsiev, Y. Losovyj, X. Zhang, P. A. Dowben, O. F. Mohammed, E. H. Sargent, and O. M. Bakr, Low trap-state density and long carrier diffusion in organolead trihalide perovskite single crystals, Science **347**, 519 (2015).
[14] L. M. Herz, Charge-carrier dynamics in organic-inorganic metal halide perovskites, Annu. Rev. Phys. Chem. **67**, 65 (2016).
[15] T. Leijtens, G. E. Eperon, A. J. Barker, G. Grancini, W. Zhang, J. M. Ball, A. R. S. Kandada, H. J. Snaith, and A. Petrozza, Carrier trapping and recombination: The role of defect physics in enhancing the open circuit voltage of metal halide perovskite solar cells, Energy Environ. Sci. **9**, 3472 (2016).
[16] X. Y. Zhu and V. Podzorov, Charge carriers in hybrid organic-inorganic lead halide perovskites might be protected as large polarons, J. Phys. Chem. Lett. **6**, 4758 (2015).
[17] K. Miyata, D. Meggiolaro, M. T. Trinh, P. P. Joshi, E. Mosconi, S. C. Jones, F. De Angelis, and X. Y. Zhu, Large polarons in lead halide perovskites, Sci. Adv. **3**, e1701217 (2017).
[18] K. Miyata and X. Y. Zhu, Ferroelectric large polarons, Nat. Mater. **17**, 379 (2018).
[19] F. Zheng and L.-W. Wang, Large polaron formation and its effect on electron transport in hybrid perovskite, Energy Environ. Sci. **12**, 1219 (2019).
[20] J. M. Frost, L. D. Whalley, and A. Walsh, Slow cooling of hot polarons in halide perovskite solar cells, ACS Energy Lett. **2**, 2647 (2017).
[21] T. Chen, W.-L. Chen, B. J. Foley, J. Lee, J. P. C. Ruff, J. Y. Peter Ko, C. M. Brown, L. W. Harriger, D. Zhang, C. Park, M. Yoon, Y.-M. Chang, J. J. Choi, and S.-H. Lee, Origin of long lifetime of band-edge charge carriers in organic-inorganic lead iodide perovskites, Proc. Natl. Acad. Sci. USA **114**, 7519 (2017).
[22] D. Cortecchia, J. Yin, A. Bruno, S.-Z. A. Lo, G. G. Gurzadyan, S. Mhaisalkar, J.-L. Brédas, and C. Soci, Polaron self-localization in white-light emitting hybrid perovskites, J. Mater. Chem. C **5**, 2771 (2017).
[23] A. J. Neukirch, W. Nie, J.-C. Blancon, K. Appavoo, H. Tsai, M. Y. Sfeir, C. Katan, L. Pedesseau, J. Even, J. J. Crochet, G. Gupta, A. D. Mohite, and S. Tretiak, Polaron stabilization by cooperative lattice distortion and cation rotations in hybrid perovskite materials, Nano Lett. **16**, 3809 (2016).
[24] J. C. Blancon, A. V. Stier, H. Tsai, W. Nie, C. C. Stoumpos, B. Traoré, L. Pedesseau, M. Kepenekian, F. Katsutani, G. T. Noe, J. Kono, S. Tretiak, S. A. Crooker, C. Katan, M. G. Kanatzidis, J. J. Crochet, J. Even, and A. D. Mohite, Scaling law for excitons in 2D perovskite quantum wells, Nat. Commun. **9**, 2254 (2018).
[25] L. Ni, U. Huynh, A. Cheminal, T. H. Thomas, R. Shivanna, T. F. Hinrichsen, S. Ahmad, A. Sadhanala, and A. Rao, Real-time observation of exciton-phonon coupling dynamics in self-assembled hybrid perovskite quantum wells, ACS Nano **11**, 10834 (2017).
[26] F. Thouin, S. Neutzner, D. Cortecchia, V. A. Dragomir, C. Soci, T. Salim, Y. M. Lam, R. Leonelli, A. Petrozza, A. R. S. Kandada, and C. Silva, Stable biexcitons in two-dimensional metal-halide perovskites with strong dynamic lattice disorder, Phys. Rev. Mater. **2**, 034001 (2018).
[27] L. Mao, Y. Wu, C. C. Stoumpos, B. Traore, C. Katan, J. Even, M. R. Wasielewski, and M. G. Kanatzidis, Tunable white-light emission in single-cation-templated three-layered 2D perovskites $(CH_3CH_2NH_3)_4Pb_3Br_{10-x}Cl_x$, J. Am. Chem. Soc. **139**, 11956 (2017).
[28] T. Hu, M. D. Smith, E. R. Dohner, M.-J. Sher, X. Wu, M. T. Trinh, A. Fisher, J. Corbett, X. -Y. Zhu, H. I. Karunadasa, and A. M. Lindenberg, Mechanism for broadband white-light emission from two-dimensional (110) hybrid perovskites, J. Phys. Chem. Lett. **7**, 2258 (2016).
[29] M. D. Smith, A. Jaffe, E. R. Dohner, A. M. Lindenberg, and H. I. Karunadasa, Structural origins of broadband emission from layered Pb-Br hybrid perovskites, Chem. Sci. **8**, 4497 (2017).
[30] D. Guo, D. Bartesaghi, H. Wei, E. M. Hutter, J. Huang, and T. J. Savenjie, Photoluminescence from radiative surface states and excitons in methylammonium lead bromide perovskites, J. Phys. Chem. Lett. **8**, 4258 (2017).
[31] A. D. Wright, C. Verdi, R. L. Milot, G. E. Eperon, M. A. Pérez-Osorio, H. J. Snaith, F. Giustino, M. B. Johnston, and L. M. Herz, Electron-phonon coupling in hybrid lead halide perovskites, Nat. Commun. **7**, 11755 (2016).
[32] H. H. Fang, L. Protesescu, D. M. Balazs, S. Adjokatse, M. V. Kovalenko, and M. A. Loi, Exciton recombination in formamidinium lead triiodide: nanocrystals versus thin films, Small **13**, 1700673 (2017).

[33] S. Tombe, G. Adam, H. Heilbrunner, D. H. Apaydin, C. Ulbricht, N. S. Sariciftci, C. J. Arendse, E. Iwuoha, and M. C. Scharber, Optical and electronic properties of mixed halide ($X = I, Cl, Br$) methylammonium lead perovskite solar cells, J. Mater. Chem. C **5**, 1714 (2017).

[34] K. Wu, A. Bera, C. Ma, Y. Du, Y. Yang, L. Li, and T. Wu, Temperature-dependent excitonic photoluminescence of hybrid organometal halide perovskite films, Phys. Chem. Chem. Phys. **16**, 22476 (2014).

[35] Z. Guo, X. Wu, T. Zhu, X. Zhu, and L. Huang, Electron-phonon scattering in atomically thin 2D perovskites, ACS Nano **10**, 9992 (2016).

[36] X. Gong, O. Voznyy, A. Jain, W. Liu, R. Sabatini, Z. Piontkowski, G. Walters, G. Bappi, S. Nokhrin, O. Bushuyev, M. Yuan, R. Comin, D. McCamant, S. O. Kelley, and E. H. Sargent, Electron-phonon interaction in efficient perovskite blue emitters, Nat. Mater. **17**, 550 (2018).

[37] O. Yaffe, Y. Guo, L. Z. Tan, D. A. Egger, T. Hull, C. C. Stoumpos, F. Zheng, T. F. Heinz, L. Kronik, M. G. Kanatzidis, J. S. Owen, A. M. Rappe, M. A. Pimenta, and L. E. Brus, Local Polar Fluctuations In Lead Halide Perovskite Crystals, Phys. Rev. Lett. **118**, 136001 (2017).

[38] K. Wang, Z. Jin, L. Liang, H. Bian, D. Bai, H. Wang, J. Zhang, Q. Wang, and S. Liu, All-inorganic cesium lead iodide perovskite solar cells with stabilized efficiency beyond 15%, Nat. Commun. **9**, 4544 (2018).

[39] K. Wang, Z. Jin, L. Liang, H. Bian, H. Wang, J. Feng, Q. Wang, and S. Liu, Chlorine doping for black γ-$CsPbI_3$ solar cells with stabilized efficiency beyond 16%, Nano Energy **58**, 175 (2019).

[40] H. Kim, J. Hunger, E. Cánovas, M. Karakus, Z. Mics, M. Grechko, D. Turchinovich, S. H. Parekh, and M. Bonn, Direct observation of mode-specific phonon-band gap coupling in methylammonium lead halide perovskites, Nat. Commun. **8**, 687 (2017).

[41] I. P. Swainson, C. Stock, S. F. Parker, L. Van Eijck, M. Russina, and J. W. Taylor, From soft harmonic phonons to fast relaxational dynamics in $CH_3NH_3PbBr_3$, Phys. Rev. B **92**, 100303(R) (2015).

[42] M. Songvilay, Z. Wang, V. G. Sakai, T. Guidi, M. Bari, Z.-G. Ye, G. Xu, K. L. Brown, P. M. Gehring, and C. Stock, Decoupled molecular and inorganic framework dynamics in $CH_3NH_3PbCl_3$, Phys. Rev. Mater. **3**, 125406 (2019).

[43] A. C. Ferreira, S. Paofai, A. Létoublon, J. Ollivier, S. Raymond, B. Hehlen, B. Rufflé, S. Cordier, C. Katan, J. Even, and P. Bourges, Direct evidence of weakly dispersed and strongly anharmonic optical phonons in hybrid perovskites, Commun. Phys. **3**, 48 (2020).

[44] G. Schuck, F. Lehmann, J. Ollivier, H. Mutka, and S. Schorr, Influence of chloride substitution on the rotational dynamics of methylammonium in $MAPbI_{3-x}Cl_x$ perovskites, J. Phys. Chem. C **123**, 11436 (2019).

[45] R. Comin, M. K. Crawford, A. H. Said, N. Herron, W. E. Guise, X. Wang, P. S. Whitfield, A. Jain, X. Gong, A. J. H. McGaughey, and E. H. Sargent, Lattice dynamics and the nature of structural transitions in organolead halide perovskites, Phys. Rev. B **94**, 094301 (2016).

[46] A. N. Beecher, O. E. Semonin, J. M. Skelton, J. M. Frost, M. W. Terban, H. Zhai, A. Alatas, J. S. Owen, A. Walsh, and S. J. L. Billinge, Direct observation of dynamic symmetry breaking above room temperature in methylammonium lead iodide perovskite, ACS Energy Lett. **1**, 880 (2016).

[47] M. A. Pérez-Osorio, Q. Lin, R. T. Phillips, R. L. Milot, L. M. Herz, M. B. Johnston, and F. Giustino, Raman spectrum of the organic-inorganic halide perovskite $CH_3NH_3PbI_3$ from first principles and high-resolution low-temperature Raman measurements, J. Phys. Chem. C **122**, 21703 (2018).

[48] M. A. Pérez-Osorio, R. L. Milot, M. R. Filip, J. B. Patel, L. M. Herz, M. B. Johnston, and F. Giustino, Vibrational properties of the organic-inorganic halide perovskite $CH_3NH_3PbI_3$ from theory and experiment: Factor group analysis, first-principles calculations, and low-temperature infrared spectra, J. Phys. Chem. C **119**, 25703 (2015).

[49] M. Park, A. J. Neukirch, S. E. Reyes-Lillo, M. Lai, S. R. Ellis, D. Dietze, J. B. Neaton, P. Yang, S. Tretiak, and R. A. Mathies, Excited-state vibrational dynamics toward the polaron in methylammonium lead iodide perovskite, Nat. Commun. **9**, 2525 (2018).

[50] K. Drużbicki, R. S. Pinna, S. Rudic, M. Jura, G. Gorini, and F. Fernandez-Alonso, Unexpected cation dynamics in the low-temperature phase of methylammonium lead iodide: The need for improved models, J. Phys. Chem. Lett. **7**, 4701 (2016).

[51] B. Li, Y. Kawakita, Y. Liu, M. Wang, M. Matsuura, K. Shibata, S. Ohira-Kawamura, T. Yamada, S. Lin, K. Nakajima, and S. Liu, Polar rotor scattering as atomic-level origin of low mobility and thermal conductivity of perovskite $CH_3NH_3PbI_3$, Nat. Commun. **8**, 16086 (2017).

[52] M. Dion, H. Rydberg, E. Schröder, D. C. Langreth, and B. I. Lundqvist, Van der Waals Density Functional For General Geometries, Phys. Rev. Lett. **92**, 246401 (2004).

[53] G. Román-Pérez and J. M. Soler, Efficient Implementation of a van der Waals Density Functional: Application to Double-Wall Carbon Nanotubes, Phys. Rev. Lett. **103**, 096102 (2009).

[54] J. Klimeš, D. R. Bowler, and A. Michaelides, Van der Waals density functionals applied to solids, Phys. Rev. B **83**, 195131 (2011).

[55] K. Lee, É. D. Murray, L. Kong, B. I. Lundqvist, and D. C. Langreth, Higher-accuracy van der Waals density functional, Phys. Rev. B **82**, 081101(R) (2010).

[56] See Supplemental Material at http://link.aps.org/supplemental/10.1103/PhysRevB.102.224310 for details of sample preparation, rotational contribution, phonon spectra analysis, and DFT calculations, in Refs. [73–87].

[57] S.-H. Lee's website: https://faculty.virginia.edu/sl5eb/research/MAPbI3_project.html.

[58] S. Grimme, Semiempirical GGA-type density functional constructed with a long-range dispersion correction, J. Comput. Chem. **27**, 1787 (2006).

[59] T. Chen, B. J. Foley, B. Ipek, M. Tyagi, J. R. D. Copley, C. M. Brown, J. J. Choi, and S.-H. Lee, Rotational dynamics of organic cations in the $CH_3NH_3PbI_3$ perovskite, Phys. Chem. Chem. Phys. **17**, 31278 (2015).

[60] Y. Q. Cheng, L. L. Daemen, A. I. Kolesnikov, and A. J. Ramirez-Cuesta, Simulation of inelastic neutron scattering spectra using OCLIMAX, J. Chem. Theory Comput. **15**, 1974 (2019).

[61] A. A. Aczel, G. E. Granroth, G. J. MacDougall, W. J. L. Buyers, D. L. Abernathy, G. D. Samolyuk, G. M. Stocks, and S. E.

Nagler, Quantum oscillations of nitrogen atoms in uranium nitride, Nat. Commun. **3**, 1124 (2012).

[62] B. Brunetti, C. Cavallo, A. Ciccioli, G. Gigli, and A. Latini, On the thermal and thermodynamic (in) stability of methylammonium lead halide perovskites, Sci. Rep. **6**, 31896 (2016).

[63] A. Gold-Parker, P. M. Gehring, J. M. Skelton, I. C. Smith, D. Parshall, J. M. Frost, H. I. Karunadasa, A. Walsh, and M. F. Toney, Acoustic phonon lifetimes limit thermal transport in methylammonium lead iodide, Proc. Natl. Acad. Sci. USA **115**, 11905 (2018).

[64] A. Miyata, A. Mitioglu, P. Plochocka, O. Portugall, J. T.-W. Wang, S. D. Stranks, H. J. Snaith, and R. J. Nicholas, Direct measurement of the exciton binding energy and effective masses for charge carriers in organic-inorganic tri-halide perovskites, Nat. Phys. **11**, 582 (2015).

[65] B. Latour and Y. Chalopin, Distinguishing between spatial coherence and temporal coherence of phonons, Phys. Rev. B **95**, 214310 (2017).

[66] C. Ge, N. Hu, P. Wu, Q. Tan, Z. Chen, Y. Wang, J. Shi, and J. Feng, Ultralow thermal conductivity and ultrahigh thermal expansion of single-crystal organic-inorganic hybrid perovskite $CH_3NH_3PbX_3$ (X = Cl, Br, I), J. Phys. Chem. C **122**, 15973 (2018).

[67] R. Heiderhoff, T. Haeger, N. Pourdavoud, T. Hu, M. Al-Khafaji, A. Mayer, Y. Chen, H.-C. Scheer, and T. Riedl, Thermal conductivity of methylammonium lead halide perovskite single crystals and thin films: A comparative study, J. Phys. Chem. C **121**, 28306 (2017).

[68] W. Lee, H. Li, A. B. Wong, D. Zhang, M. Lai, Y. Yu, Q. Kong, E. Lin, J. J. Urban, J. C. Grossman, and P. Yang, Ultralow thermal conductivity in all-inorganic halide perovskites, Proc. Natl. Acad. Sci. USA **114**, 8693 (2017).

[69] A. Pisoni, J. Jaćimović, O. S. Barišić, M. Spina, R. Gaál, L. Forró, and E. Horváth, Ultra-low thermal conductivity in organic-inorganic hybrid perovskite $CH_3NH_3PbI_3$, J. Phys. Chem. Lett. **5**, 2488 (2014).

[70] X. Qian, X. Gu, and R. Yang, Lattice thermal conductivity of organic-inorganic hybrid perovskite $CH_3NH_3PbI_3$, Appl. Phys. Lett. **108**, 063902 (2016).

[71] T. Takabatake, K. Suekuni, T. Nakayama, and E. Kaneshita, Phonon-glass electron-crystal thermoelectric clathrates: Experiments and theory, Rev. Mod. Phys. **86**, 669 (2014).

[72] A. Giri, A. Z. Chen, A. Mattoni, K. Aryana, D. Zhang, X. Hu, S.-H. Lee, J. J. Choi, and P. E. Hopkins, Ultralow thermal conductivity of two-dimensional metal halide perovskites, Nano Lett. **20**, 3331 (2020).

[73] H. Zhu, K. Miyata, Y. Fu, J. Wang, P. P. Joshi, D. Niesner, K. W. Williams, S. Jin, and X.-Y. Zhu, Screening in crystalline liquids protects energetic carriers in hybrid perovskites, Science **353**, 1409 (2016).

[74] D. L. Abernathy, M. B. Stone, M. J. Loguillo, M. S. Lucas, O. Delaire, X. Tang, J. Y. Y. Lin, and B. Fultz, Design and operation of the wide angular-range chopper spectrometer ARCS at the spallation neutron source, Rev. Sci. Instrum. **83**, 015114 (2012).

[75] R. T. Azuah, L. R. Kneller, Y. Qiu, P. L. W. Tregenna-Piggott, C. M. Brown, J. R. D. Copley, and R. M. Dimeo, DAVE: A comprehensive software suite for the reduction, visualization, and analysis of low energy neutron spectroscopic data, J. Res. Natl. Inst. Stand. Technol. **114**, 341 (2009).

[76] R. Kajimoto, M. Nakamura, Y. Inamura, F. Mizuno, K. Nakajima, S. Ohira-Kawamura, T. Yokoo, T. Nakatani, R. Maruyama, K. Soyama, K. Shibata, K. Suzuya, S. Sato, K. Aizawa, M. Arai, S. Wakimoto, M. Ishikado, S. Shamoto, M. Fujita, H. Hiraka *et al.*, The Fermi chopper spectrometer 4SEASONS at J-PARC, J. Phys. Soc. Jpn. **80**, SB025 (2011).

[77] M. Nakamura, R. Kajimoto, Y. Inamura, F. Mizuno, M. Fujita, T. Yokoo, and M. Arai, First demonstration of novel method for inelastic neutron scattering measurement utilizing multiple incident energies, J. Phys. Soc. Jpn. **78**, 093002 (2009).

[78] M. Bée, *Quasielastic Neutron Scattering: Principles and Applications in Solid State Chemistry, Biology and Materials Science* (Adam Hilger, Bristol, UK, 1988).

[79] G. Kresse and J. Furthmüller, Efficient iterative schemes for *ab initio* total-energy calculations using a plane-wave basis set, Phys. Rev. B **54**, 11169 (1996).

[80] G. Kresse and D. Joubert, From ultrasoft pseudopotentials to the projector augmented-wave method, Phys. Rev. B **59**, 1758 (1999).

[81] J. P. Perdew, K. Burke, and M. Ernzerhof, Generalized Gradient Approximation Made Simple, Phys. Rev. Lett. **77**, 3865 (1996).

[82] G. Kresse, J. Furthmüller, and J. Hafner, *Ab initio* force constant approach to phonon dispersion relations of diamond and graphite, EPL **32**, 729 (1995).

[83] K. Parlinski, Z. Q. Li, and Y. Kawazoe, First-Principles Determination of the Soft Mode in Cubic ZrO_2, Phys. Rev. Lett. **78**, 4063 (1997).

[84] A. Togo and I. Tanaka, First principles phonon calculations in materials science, Scr. Mater. **108**, 1 (2015).

[85] D. C. Wallace, *Thermodynamics of Crystals* (Courier Corporation, New York, 1998).

[86] G. L. Squires, *Introduction to the Theory of Thermal Neutron Scattering* (Cambridge University Press, Cambridge, 2012).

[87] A. Togo, Phonopy examples, https://github.com/atztogo/phonopy/tree/master/example/ (2019).